Indian Journal of Pure & Applied Physics
Vol. 64, April 2026, pp. 358-368
DOI: 10.56042/ijpap.v64i4.20494

Thermal Analysis of CuO–MoS_2–TiO_2/Water Ternary Hybrid Nanofluid Flow over a Rotating Disk with Joule Heating and Viscous Dissipation

M Barkathunnisa[a], M Chitra[a] & B Rushi Kumar[b*]

[a]Department of Mathematics, Thiruvalluvar University, Serkkadu, Vellore 632 115, Tamil Nadu, India

[b]Department of Mathematics, School of Advanced Sciences, Vellore Institute of Technology, Vellore 632 014, Tamil Nadu, India

Received: 9th June 2025; accepted: 19th February 2026

The CuO-MoS_2-TiO_2/water ternary hybrid nanofluid flow over a rotating disk is examined in this study with respect to its thermal and flow characteristics, considering the combined influences of a magnetic field, Hall current, thermal radiation, Joule heating, viscous dissipation, and a non-uniform heat source/sink. Along with velocity and thermal slip boundary conditions, the flow system also takes Darcy-Forchheimer drag into account. The bvp4c solver in MATLAB is used to solve the governing nonlinear partial differential equations numerically after they have been simplified using Von Kármán similarity transformations. The effects of several physical parameters on temperature and velocity profiles are investigated through a comprehensive parametric analysis. The findings show that porous resistance and magnetic fields improve thermal dispersion through Joule heating while suppressing fluid mobility. Additionally, the presence of the Hall current promotes radial fluid motion, even though it leads to a reduction in both axial and tangential velocity components. The findings reveal that the ternary hybrid nanofluid delivers superior thermal performance in comparison with both mono and hybrid nanofluids. An evaluation based on the Nusselt number shows that the heat transfer rate improves by nearly 18 to 25 % over mono nanofluids and 10 to 15 % over hybrid nanofluids when the operating conditions are kept unchanged. Furthermore, enhancement in nanoparticle loading and thermal radiation parameters result in an additional 6 to 33 % rise in heat transfer, highlighting the effective synergistic thermal behaviour produced by the combined presence of three nanoparticles.

Keywords: Ternary hybrid nanofluid, Thermal radiation, Hall current, Darcy forchheimer, Heat source/sink, Joule heating

1 Introduction

Nanofluids, formed by dispersing solid nanoparticles into conventional base fluids, have attracted considerable attention due to their enhanced thermal transport characteristics compared to ordinary fluids[1]. Early investigations demonstrated that even a small amount of nanoparticles can significantly improve heat transfer performance, motivation extensive research into their applications in energy systems, cooling technologies, and thermal management devices[2,3]. However, mono nanofluids often suffer from stability limitations and restricted thermal enhancement, which has encouraged researchers to explore more advanced formulations[4].

To overcome these limitations, hybrid nanofluids consisting of two different nanoparticles suspended in a base fluid were introduced and shown to exhibit superior thermophysical properties due to synergistic effects between the nanoparticles[5,6]. Further advancement led to the development of ternary hybrid nanofluids, which integrate three distinct nanoparticles to achieve improved thermal conductivity, rheological behaviour, and operational stability[7]. These fluids have demonstrated remarkable potential in high performance thermal systems where enhanced heat transfer is essential[8, 9].

Among various base fluids, water is widely used because of its favourable thermal properties, availability, and compatibility with a broad range of nanoparticles[10]. In particular, the CuO-MoS_2-TiO_2/water ternary hybrid nanofluid emerged as a promising working fluid due to the combined advantages of its constituents. Copper oxide (CuO) offers high thermal conductivity, molybdenum disulphide (MoS_2) contributes excellent lubrication and thermal stability, and titanium dioxide (TiO_2) enhances chemical stability and dispersion characteristics[11-13].

Rotating disk systems are frequently encountered in engineering applications such as turbines, chemical reactors, hard disk drives, and cooling of rotating machinery[14]. The classical rotating disk flow problem initially formulated using the Von Karman similarity approach, provides a fundamental framework for

*Corresponding author: E-mail: rushikumar@vit.ac.in

analysing transport phenomena in such configurations[15]. When rotation is combined with electrically conducting fluids, magnetohydrodynamic (MHD) effects become significant and can be utilized to control flow behaviour and heat transfer rates[16].

The inclusion of Hall current effects further modifies the flow structure, particularly under strong magnetic fields, leading to notable changes in velocity components and thermal characteristics[17]. Additionally, thermal radiation plays a crucial role in high-temperature distribution within the boundary layer[18]. Internal heat generation or absorption mechanisms are also important in modelling realistic energy systems, as they directly affect thermal performance[19].

In practical rotating disk configurations, inertial effects become non-negligible, especially at higher rotational speeds. The Darcy-Forchheimer model is therefore employed to accurately describe flow resistance in porous or semi-porous media by accounting for both viscous and inertial drag forces[20, 21]. Joule heating, arising from the interaction between the magnetic field and induced electric currents, further contributes to thermal energy within the fluid and must be considered for precise thermal analysis[22].

Motivated by the above considerations, the present study investigates the MHD flow and heat transfer characteristics of a CuO-MoS_2-TiO_2/water ternary hybrid nanofluid over a rotating disk, incorporating the effects of Hall current, thermal radiation, Darcy-Forchheimer resistance, heat source/sink, and Joule heating. To the best of the authors' knowledge, a comprehensive analysis combining all these effects for a ternary hybrid nanofluid in a rotating disk configuration remains limited in the existing literature[23].

2 Materials and Methods

The axisymmetric, steady, and incompressible MHD flow of ternary hybrid nanofluid over a disk rotating about the z-axis with a constant angular velocity Ω is considered, as shown in Fig. 1. The flow is described in cylindrical coordinates (r, φ, z), where the radial, tangential, and axial directions correspond to the respective velocity components. The ternary hybrid nanofluid composed of CuO-MoS_2-TiO_2 nanoparticles dispersed in a base fluid, is exposed to a uniform magnetic field applied along the z-direction. The analysis includes the effects of thermal radiation, Hall current, Joule heating, and viscous dissipation to capture the combined influence of electromagnetic

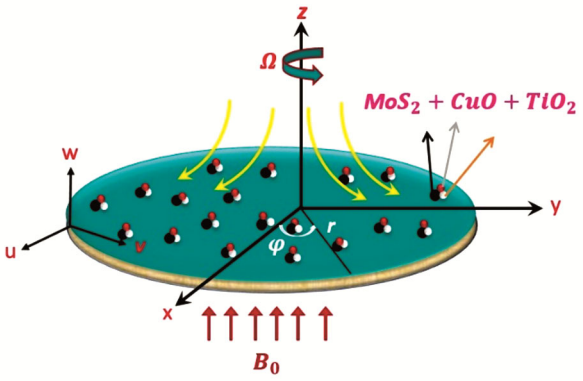

Fig. 1 — Flow Diagram

and thermal mechanisms. Thermal equilibrium between the base fluid and nanoparticles is assumed, allowing the suspension to be treated as a single-phase homogeneous medium with effective thermophysical properties. Radiative heat transfer is modelled using Rosseland diffusion approximation, while uniform nanoparticle dispersion without agglomeration is assumed to ensure physical consistency and mathematical tractability.

The Eqs. are[24, 25, 26]

$$\frac{\partial u}{\partial r}+\frac{u}{r}+\frac{\partial w}{\partial z}=0 \quad \ldots (1)$$

$$u\frac{\partial u}{\partial r}-\frac{v^2}{r}+w\frac{\partial u}{\partial z}+\frac{1}{\rho_{thnf}}\frac{\partial p}{\partial r}=\frac{\mu_{thnf}}{\rho_{thnf}}\left(\frac{\partial^2 u}{\partial r^2}+\frac{1}{r}\frac{\partial u}{\partial r}-\frac{u}{r^2}+\frac{\partial^2 u}{\partial z^2}\right)-\frac{\mu_{thnf}}{\rho_{thnf}K}u-Fu^2-\frac{\sigma_{thnf}B_0^2}{\rho_{thnf}(1+m^2)}(u-mv) \quad \ldots (2)$$

$$u\frac{\partial v}{\partial r}+\frac{uv}{r}+w\frac{\partial v}{\partial z}=\frac{\mu_{thnf}}{\rho_{thnf}}\left(\frac{\partial^2 v}{\partial r^2}+\frac{1}{r}\frac{\partial v}{\partial r}-\frac{v}{r^2}+\frac{\partial^2 v}{\partial z^2}\right)-\frac{\mu_{thnf}}{\rho_{thnf}K}v-Fv^2-\frac{\sigma_{thnf}B_0^2}{\rho_{thnf}(1+m^2)}(v+mu) \quad \ldots (3)$$

$$u\frac{\partial T}{\partial r}+w\frac{\partial T}{\partial z}=\frac{k_{thnf}}{(\rho c_p)_{thnf}}\left(\frac{\partial^2 T}{\partial r^2}+\frac{1}{r}\frac{\partial T}{\partial r}+\frac{\partial^2 T}{\partial z^2}\right)-\frac{1}{(\rho c_p)_{thnf}}\frac{\partial q_r}{\partial z}+\frac{1}{(\rho c_p)_{thnf}}Q_0(T-T_\infty)+\frac{\sigma_{thnf}B_0^2}{(\rho c_p)_{thnf}(1+m^2)}(u^2+v^2)+\frac{\mu_{thnf}}{(\rho c_p)_{thnf}}\left(\left(\frac{\partial u}{\partial z}\right)^2+\left(\frac{\partial v}{\partial z}\right)^2\right) \quad \ldots (4)$$

The boundary conditions are:

$$u=\gamma'\frac{\partial u}{\partial z}, v=\Omega r+\gamma'\frac{\partial v}{\partial z}, w=0, T=T_w+\delta'\frac{\partial T}{\partial z}\ at\ z=0, \text{ and}$$
$$u\to 0, v\to 0, T\to T_\infty, p\to p_\infty\ at\ z\to\infty \quad \ldots (5)$$

The boundary conditions presented in Eq. (5) accurately represent the physical problem of a rotating disk with specific characteristics. At the disk surface ($z=0$), the no-slip condition is applied for the radial velocity component (u), while the tangential velocity (v) matches the disk rotation (Ωr), accounting for the slip effect through the parameter γ in the velocity derivative term. The axial velocity ($w=0$) represents

the impermeability condition at the solid disk surface, while the thermal boundary condition incorporates the slip effect through the parameter δ in the temperature gradient. At the free stream ($z \to \infty$), all velocity components vanish and temperature approaches the ambient value, which is physically consistent with the flow decaying far from the rotating disk. These boundary conditions are standard for rotating disk problems with slip effects and have been validated in numerous studies. The slip parameters γ and δ allow us to investigate various physical scenarios ranging from no-slip to partial slip conditions, making the model applicable to practical engineering situations where surface roughness or special coatings influence the flow behavior.

Here, K represents the Darcy permeability of the porous medium, and p_∞ denotes the pressure of the nanofluids at infinity.

The convective heat flux q_r is expressed as

$$q_r = -\frac{4\sigma^*}{3k^*}\frac{\partial T^4}{\partial z} = -\frac{16\sigma^* T_\infty^3}{3k^*}\frac{\partial T}{\partial z}, \text{ where } T^4 = 4TT_\infty^3 - 3T_\infty^4 \quad \ldots (6)$$

where $\sigma^*$and k^* exemplifies Stefen-Boltzman constant and mean absorption coefficient, respectively.

Consider Von Karman's transformations[27]

$$\eta = \left(\frac{\Omega}{v_f}\right)^{\frac{1}{2}} z, u = \Omega r F(\eta), v = \Omega r G(\eta), w = \left(\Omega v_f\right)^{\frac{1}{2}} H(\eta), p - p_\infty = 2\mu_f \Omega p(\eta), \theta(\eta) = \frac{T - T_\infty}{T_w - T_\infty} \quad \ldots (7)$$

By applying the above transformations to Eqs. (1) -(4), we obtain

$$H'(\eta) + 2F(\eta) = 0 \quad \ldots (8)$$

$$\frac{A_1}{A_2}F''(\eta) - \frac{A_3}{A_2}M[F(\eta) - mG(\eta)] - H(\eta)F'(\eta) - Fr\left(F^2(\eta)\right) - F^2(\eta) + G^2(\eta) - \frac{A_1}{A_2}F(\eta)K_1 = 0 \quad \ldots (9)$$

$$\frac{A_1}{A_2}G''(\eta) - H(\eta)G'(\eta) - \frac{A_3}{A_2}M[G(\eta) + mF(\eta)] - Fr\left(G^2(\eta)\right) - 2F(\eta)G(\eta) - \frac{A_1}{A_2}G(\eta)K_1 = 0 \quad \ldots (10)$$

$$(A_5 + Rd)\theta''(\eta) - A_4 \Pr[H(\eta)\theta'(\eta)] + PrQ\theta(\eta) + A_3 MPrEc[F^2(\eta) + G^2(\eta)] + A_1 EcPr[F'^2(\eta) + G'^2(\eta)] = 0 \quad \ldots (11)$$

Here the functions $F(\eta), G(\eta),$ and $H(\eta)$ denote the velocity components along the radial, tangential, and axial directions, respectively, while $\theta(\eta)$ describes the dimensionless temperature profile. The porosity parameter is expressed as $K_1 = \mu_f/(K\Omega\rho_f)$, the slip velocity coefficient is given by $\gamma = \gamma'/\sqrt{\Omega/v_f}$, and the thermal slip coefficient is represented by $\delta = \delta'/\sqrt{\Omega/v_f}$.

Furthermore, the non-dimensional parameters accounting for various physical effects are defined as follows: the magnetic field parameter$M = \frac{\sigma_f B_0^2}{\rho_f \Omega(1+m^2)}$, the thermal radiation parameter $Rd = \frac{4\sigma^* T_\infty^3}{k^* k_f}$, the Prandtl number $Pr = \frac{\mu_f (\rho C_p)_f}{\rho_f k_f}$, the Eckert number $Ec = \frac{\rho_f r^2 \Omega^2}{(\rho C_p)_f \Omega(T_w - T_\infty)}$, the Darcy-Forchheimer term $Fr = \frac{C_b}{\sqrt{k}}$, and the non-uniform heat source/sink parameter $Q = \frac{Q_0}{\Omega(\rho C_p)_f}$.

Ternary hybrid nanofluids thermophysical characteristics[28] are as follows:

$$A_1 = \frac{\mu_{thnf}}{\mu_f} = \frac{1}{(1-\varphi_1-\varphi_2-\varphi_3)^{2.5}} \quad \ldots (12)$$

$$A_2 = \frac{\rho_{thnf}}{\rho_f} = (1-\varphi_1)\left((1-\varphi_2)\left[(1-\varphi_3) + \varphi_3\frac{\rho_{s3}}{\rho_f}\right] + \varphi_2\left(\frac{\rho_{s2}}{\rho_f}\right)\right) + \varphi_1\left(\frac{\rho_{s1}}{\rho_f}\right) \quad \ldots (13)$$

$$A_3 = \frac{\sigma_{thnf}}{\sigma_{hnf}} = \frac{\sigma_{s1}(1+2\varphi_1) + \sigma_{hnf}(1-2\varphi_1)\varphi_1 + \sigma_{s2}\varphi_2}{\sigma_{s1}(1-\varphi_1) + \sigma_{hnf}(1-\varphi_1)}, \frac{\sigma_{hnf}}{\sigma_{nf}} = \frac{\sigma_{s2}(1+2\varphi_2) + \sigma_{nf}(1-2\varphi_2)}{\sigma_{s2}(1-\varphi_2) + \sigma_{nf}(1-\varphi_2)}, \frac{\sigma_{nf}}{\sigma_f} = \frac{\sigma_{s3}(1+2\varphi_3) + \sigma_f(1-2\varphi_3)}{\sigma_{s3}(1-\varphi_3) + \sigma_f(1-\varphi_3)} \quad \ldots (14)$$

$$A_4 = \frac{(\rho C_p)_{thnf}}{(\rho C_p)_f} = \varphi_1\left(\frac{(\rho C_p)_{s1}}{(\rho C_p)_f}\right) + (1-\varphi_1)\left[(1-\varphi_2)\left((1-\varphi_3) + \varphi_3\left(\frac{(\rho C_p)_{s3}}{(\rho C_p)_f}\right)\right) + \varphi_2\left(\frac{(\rho C_p)_{s2}}{(\rho C_p)_f}\right)\right] \quad \ldots (15)$$

$$A_5 = \frac{k_{thnf}}{k_{hnf}} = \frac{k_{s1} + 2k_{hnf} - 2\varphi_1(k_{hnf} - k_{s1})}{k_{s1} + 2k_{hnf} + \varphi_1(k_{hnf} - k_{s1})}, \frac{k_{hnf}}{k_{nf}} = \frac{k_{s2} + 2k_{nf} - 2\varphi_2(k_{nf} - k_{s2})}{k_{s2} + 2k_{nf} + \varphi_2(k_{nf} - k_{s2})}, \frac{k_{nf}}{k_f} = \frac{k_{s3} + 2k_f - 2\varphi_3(k_f - k_{s3})}{k_{s3} + 2k_f + \varphi_3(k_f - k_{s3})} \quad \ldots (16)$$

The boundary conditions (7) become

$$F(0) = \gamma F'(0), G(0) = 1 + \gamma G'(0), H(0) = 0, \theta(0) = 1 + \delta\theta'(0), F(\infty) = G(\infty) = \theta(\infty) = p(\infty) = 0 \quad \ldots (17)$$

The physical parameters introduced include the coefficient of friction C_f and the Nusselt number Nu, defined as:

$$C_f = \frac{\sqrt{\tau_{wr}^2 + \tau_{w\varphi}^2}}{\rho_f(\Omega r)^2} \text{ and } Nu = \frac{r q_w}{k_f(T_w - T_\infty)} \quad \ldots (18)$$

where τ_{wr} and $\tau_{w\varphi}$ represent the shear stress in the radial and tangential directions at the disk's surface, respectively, and q_w is surface heat flux. These are described as follows:

$$\tau_{wr} = \left[\mu_{thnf}(u_z + w_\varphi)\right]_{z=0}, \tau_{w\varphi} = \left[\mu_{thnf}(v_z + \frac{1}{r}w_\varphi)\right]_{z=0}, q_w = -\left[k_{thnf} + \frac{16\sigma^* T_\infty^3}{3k^*}\right]\left(\frac{\partial T}{\partial z}\right)_{z=0} \quad \ldots (19)$$

By applying Eqs. (7) - (19), Eq. (18) becomes

$$Re^{\frac{1}{2}}C_f = \frac{\sqrt{F'(0)^2+G'(0)^2}}{(1-\varphi_1)^{2.5}(1-\varphi_2)^{2.5}(1-\varphi_3)^{2.5}}, Re^{-\frac{1}{2}}Nu = -(A_5+Rd)\theta'(0) \quad \ldots (20)$$

2.1 Procedure for Numerical Solutions

The numerical solution of Eqs. (8) – (11), subject to boundary conditions in Eq. (17), is carried out using MATLAB's bvp4c solver. The methodology employed in this approach is schematically represented in Fig. 2. This diagram provides a structured overview of the solution process, beginning with the conversion of the original higher order nonlinear differential equations into an equivalent system of first-order ordinary differential equations through the introduction of appropriate variables. The flow chart also illustrates key steps such as the application of boundary conditions, domain discretization, the generation of initial guesses, and the iterative solution process. These steps ultimately lead to the computation of velocity and temperature distributions for the ternary hybrid nanofluid flow over the rotating disk.

For the numerical implementation, the bvp4c function is executed with a relative tolerance of 10^{-6} and an absolute tolerance of 10^{-8}. Convergence of the numerical scheme is verified by ensuring that successive iterations exhibit negligible changes in the solution profiles as well as in the derived engineering quantities, including the skin friction coefficients and the Nusselt number. The far-field boundary η_∞ is selected sufficiently large to guarantee accurate satisfaction of the asymptotic boundary conditions.

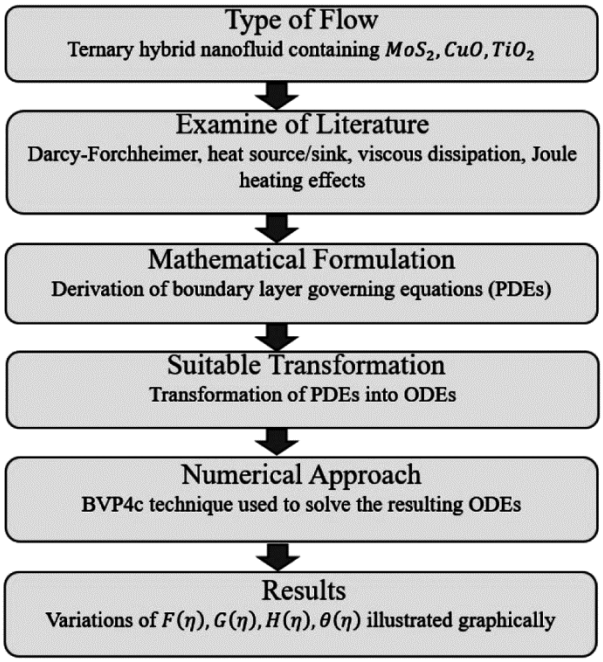

Fig. 2 — Flow Chart

$$F = u_1, F' = u_2, F'' = u_2', H = u_3, H' = u_3', G = u_4, G' = u_5, G'' = u_5', \theta = u_6, \theta' = u_7, \theta'' = u_7' \quad \ldots (21)$$

$$u_2' = \frac{A_3}{A_1}M(u_1 - mu_4) + \frac{A_2}{A_1}(u_3u_2 + Fru_1^2 + u_1^2 - u_4^2) + u_1K_1 \quad \ldots (22)$$

$$u_5' = \frac{A_2}{A_1}(u_3u_5 + 2u_1u_4 + Fru_4^2) + \frac{A_3}{A_1}M(u_4 + mu_1) + u_4K_1 \quad \ldots (23)$$

$$u_3' = -2u_1 \quad \ldots (24)$$

$$u_7' = \frac{Pr}{A_5+Rd}\left(A_4u_3u_7 - Qu_6 - A_3MEc(u_1^2+u_4^2)\right) - A_1Ec(u_2^2+u_5^2) \quad \ldots (25)$$

In this formulation, the boundary conditions become

$$u_1(0) = \gamma u_2(0), u_4(0) = 1 + \gamma u_5(0), u_3(0) = 0,\ u_6(0) = 1 + \delta u_7(0), \text{ and } u_1(\infty) = u_4(\infty) = u_6(\infty) = 0. \quad \ldots (26)$$

3 Results and Discussion

This study presents numerical solutions for the nonlinear differential Eqs. (8) – (11) using MATLAB's bvp4c solver, subject to the boundary conditions given in Eq. (17). This investigation focuses on evaluating the velocity and temperature distributions of a ternary hybrid nanofluid across a specified range of governing parameters. The results are illustrated through various graphs and supported by tabulated data, while the thermophysical characteristics of the base fluid and nanoparticles are summarized in Table 1. To ensure the accuracy of the numerical scheme, key quantities namely $F'(0), -G'(0), -H(\infty)\ and\ -\theta'(0)$ are evaluated and compared with reference results from Yin et al. (2015), as reported in Table 2. The data are obtained for the parameter values: $Pr = 6.2, M = 0.1, Rd = 0.1, m = 0.1, K_1 = 0.1, \gamma = 0.1, \delta = 0.1, \varphi_1 = 0.01, \varphi_2 = 0.01, \varphi_3 = 0.01, Ec = 0.1, Q = 0.1, and\ Fr = 0.1.$

Table 1 — Thermophysical properties of nanoparticles[29, 30]

Physical properties	Base fluid (Water)	Copper Oxide (*CuO*)	Molybdenum Disulfide (MoS_2)	Titanium dioxide (TiO_2)
Density $\rho(kg/m^3)$	997.1	6320	5060	4250
Thermal conductivity $k(W/mK)$	0.613	76.5	904.4	8.9538
Specific heat capacity $C_p(J/kgK)$	4179	531.8	397.4	686.2
Electric conductivity $\sigma(\Omega m)^{-1}$	0.05	2.7×10^{-8}	2.1×10^{-6}	1×10^{-12}

Figures 3 (a–d) explore the influence of the magnetic parameter M on the velocity and temperature profiles. As M increases, the radial velocity, tangential velocity G, and axial velocity Hall decrease. This behavior is due to the Lorentz force generated by the magnetic field, which acts as a resistive force opposing the motion of the fluid in all directions. In contrast, the temperature θ increases with M, owing to the intensified Joule heating that contributes additional thermal energy to the boundary layer.

Figures 4 (a–c) illustrate the effect of the velocity slip parameter γ on the velocity field. An increase in γ leads to a decrease in the radial velocity F and tangential velocity G, while the axial velocity H increases. This indicates that slip at the rotating surface reduces shear stress and weakens momentum transfer in the radial and tangential directions. However, the axial component increases, likely due to a redistribution of the fluid flow resulting from reduced shear resistance near the wall.

Figure 5 shows the effect of the thermal slip parameter δ on the temperature profile θ. As δ increases, the temperature θ also increases. This behavior occurs because a higher thermal slip parameter reduces the resistance to heat flow at the surface, allowing more thermal energy to be transferred from the rotating disk into the fluid. As a result, the fluid temperature within the boundary layer rises.

Figures 6 (a–d) illustrate the impact of the porosity parameter on the flow and thermal fields. As K_1 increases, the radial velocity F and tangential velocity G decrease due to increased resistance within the porous medium. Meanwhile, the axial velocity H and temperature θ both increase. The rise in H is attributed to the fluid being redirected in the axial direction, while the elevated θ results from diminished convective cooling, allowing more heat to accumulate within the fluid.

Table 2 − Comparison of values for $F'(0), -G'(0), -H(\infty)$ and $-\theta'(0)$ with parameters set to $Pr = 6.2, \varphi = 0, m = 0, M = 0, \gamma = 0, \delta = 0, Rd = 0, K_1 = 0, Q = 0, Fr = 0$ and $Ec = 0$

Quantity	Yin *et al*. (2015)	Present Results
$F'(0)$	0.51022941	0.5101165
$-G'(0)$	0.61591990	0.61584931
$-H(\infty)$	0.88446912	0.87461518
$-\theta'(0)$	0.93387285	0.93369411

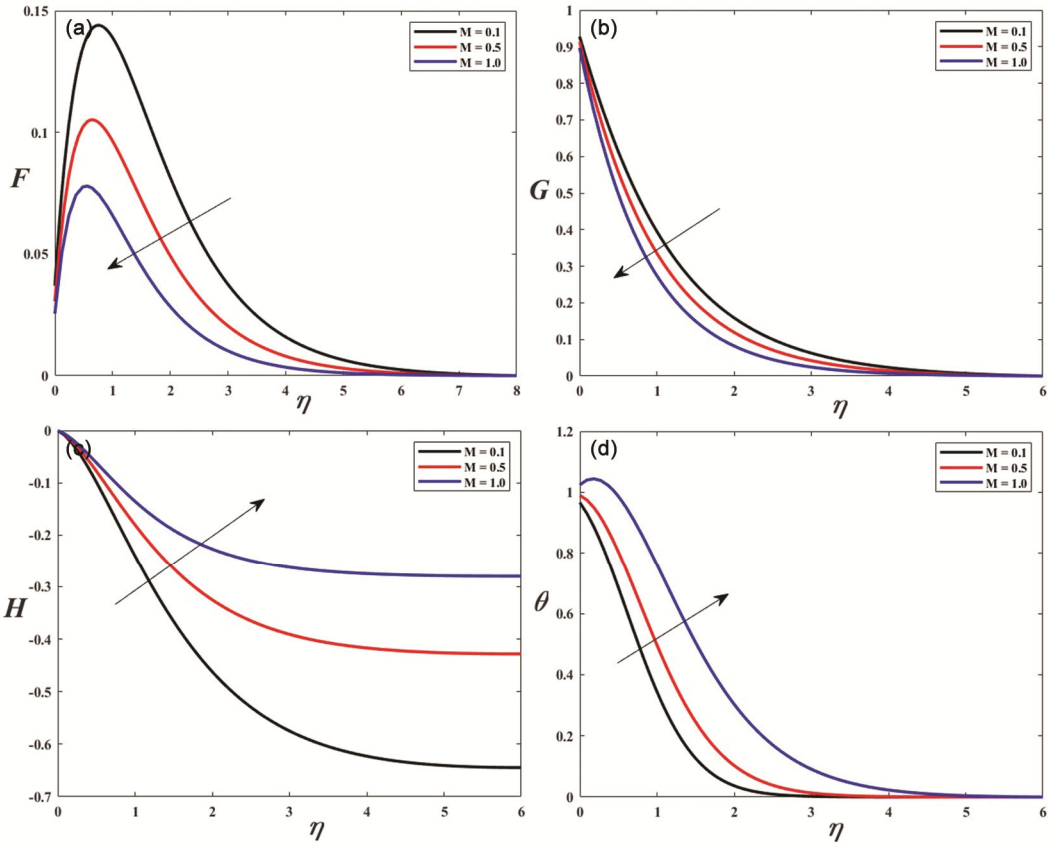

Fig. 3 — (a) Impact of M on F (b) Impact of M on G (c) Impact of M on H; and (d) Impact of M on θ

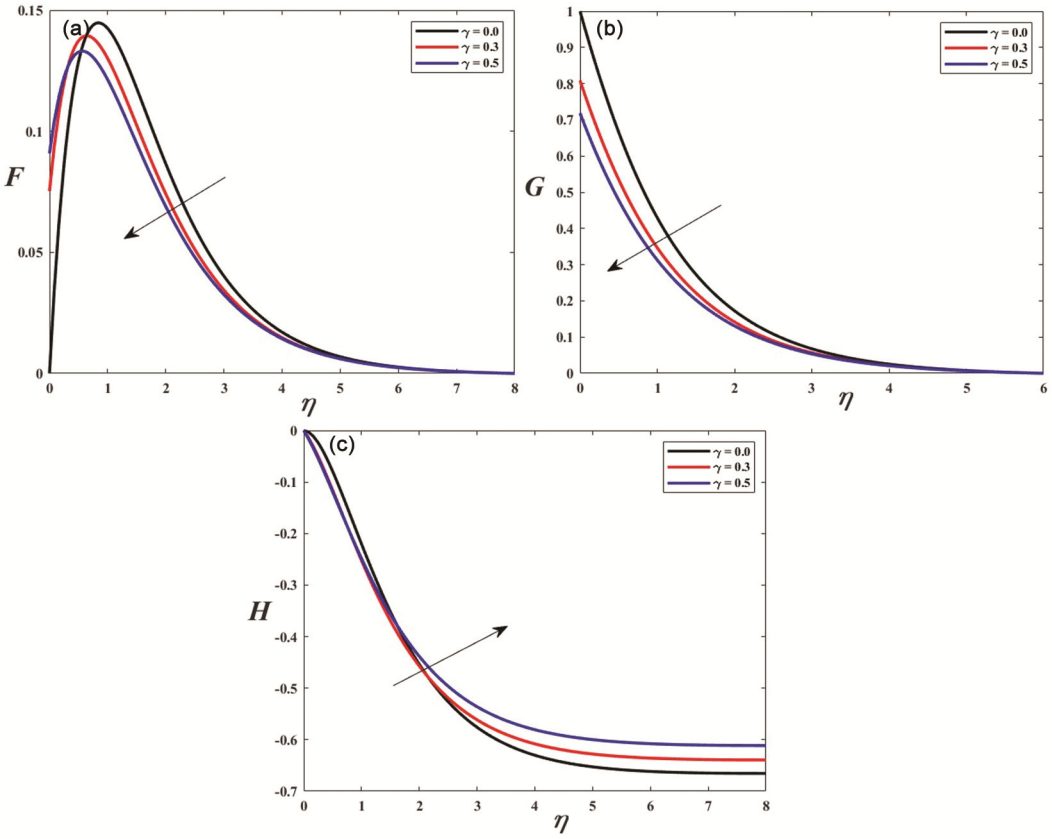

Fig. 4 — (a) Impact of γ on F (b) Impact of γ on G; and (c) Impact of γ on H

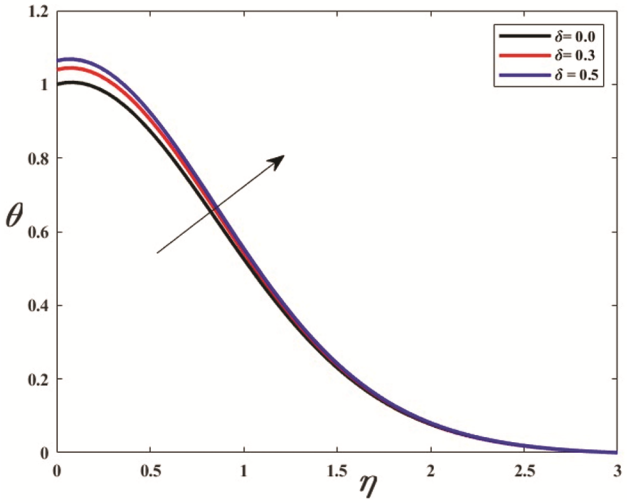

Fig. 5 — Impact of δ on θ

Figures 7 (a–d) depict the influence of the Hall current parameter m on the system. With increasing m, the radial velocity F increases, while the tangential velocity G, axial velocity H, and temperature θ decrease. The Hall current introduces a force component that boosts radial motion. However, it simultaneously alters the current paths in the fluid, leading to reductions in G and H. The temperature decreases as enhanced convective transport under the Hall effect facilitates more efficient heat removal from the system.

Figures 8 (a–d) demonstrate the effect of the Darcy–Forchheimer parameter Fr on the velocity and temperature profiles. An increase in Fr leads to a reduction in the radial velocity F and tangential velocity G due to stronger inertial and porous drag effects. In contrast, the axial velocity H and temperature θ increase. The rise in H suggests a directional shift of the flow, and the increase in θ is due to the resistive forces converting mechanical energy into thermal energy within the boundary layer.

Figure 9 presents the influence of the Joule heating parameter, represented by the Eckert number Ec on the temperature profile θ. As Ec increases, θ also rises, as more viscous dissipation and Joule heating convert kinetic and electrical energy into internal energy, resulting in a higher fluid temperature and a thicker thermal boundary layer.

Figure 10 shows the effect of the thermal radiation parameter Rd on temperature. It is observed that an increase in Rd raises the temperature θ. This happens

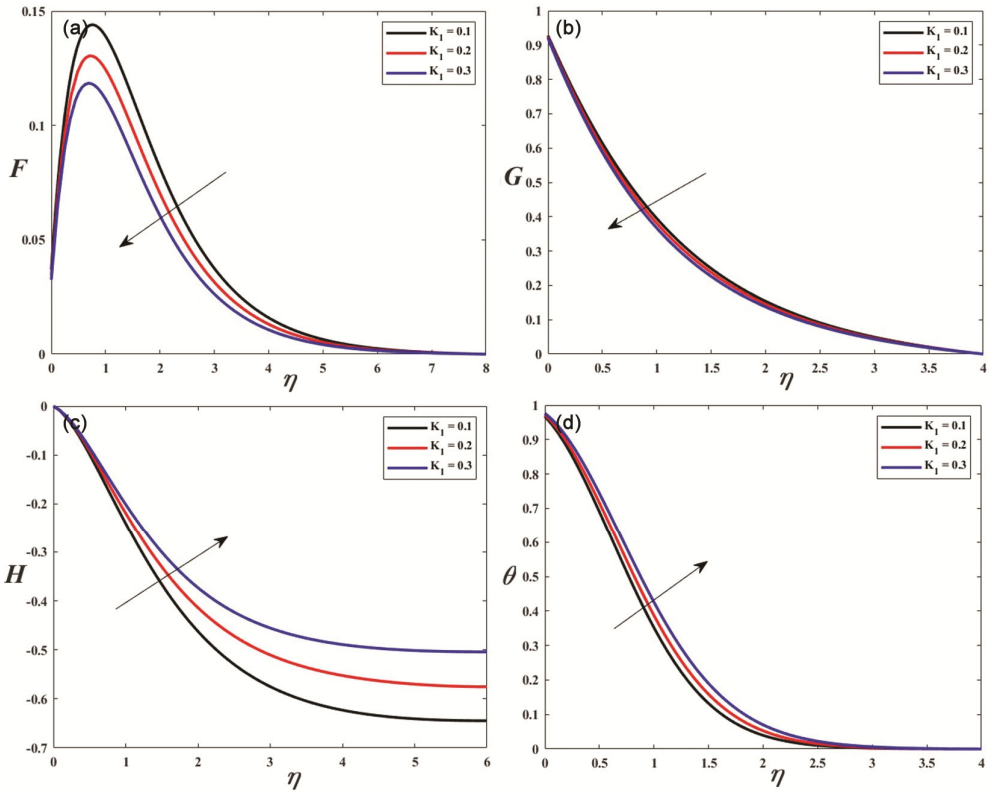

Fig. 6 — (a) Impact of K_1 on F (b) Impact of K_1 on G (c) Impact of K_1 on H; and (d) Impact of K_1 on θ

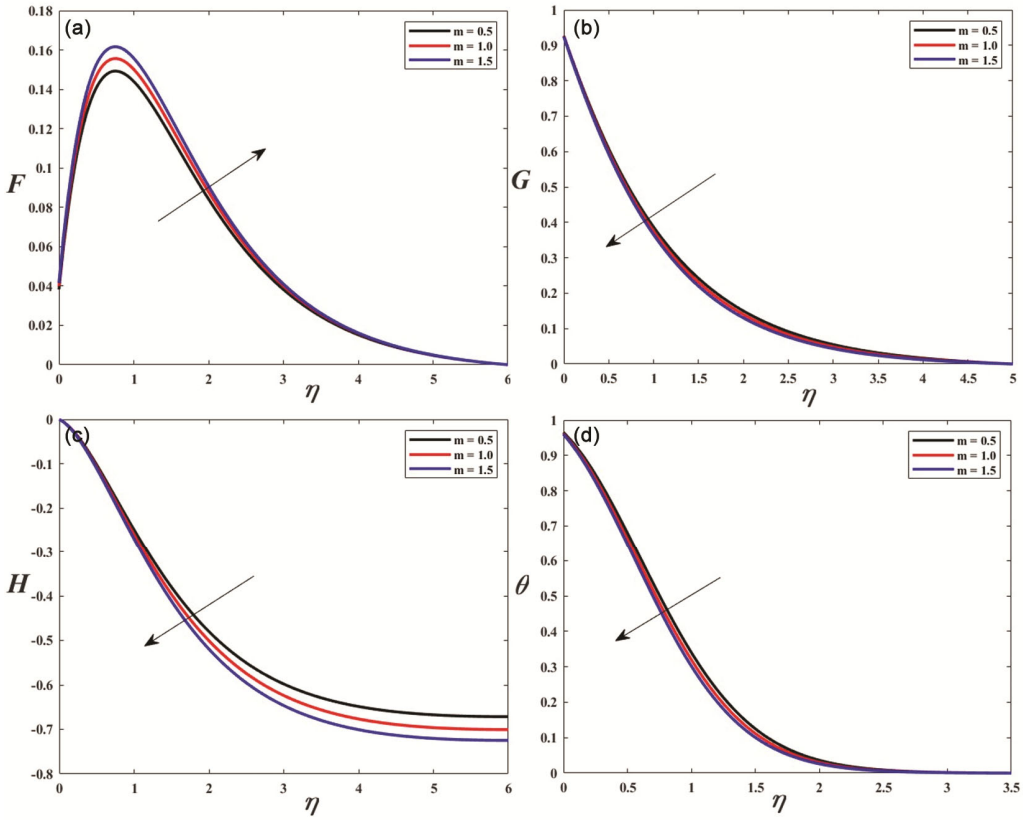

Fig. 7 — (a) Impact of m on F (b) Impact of m on G (c) Impact of m on H; and (d) Impact of m on θ

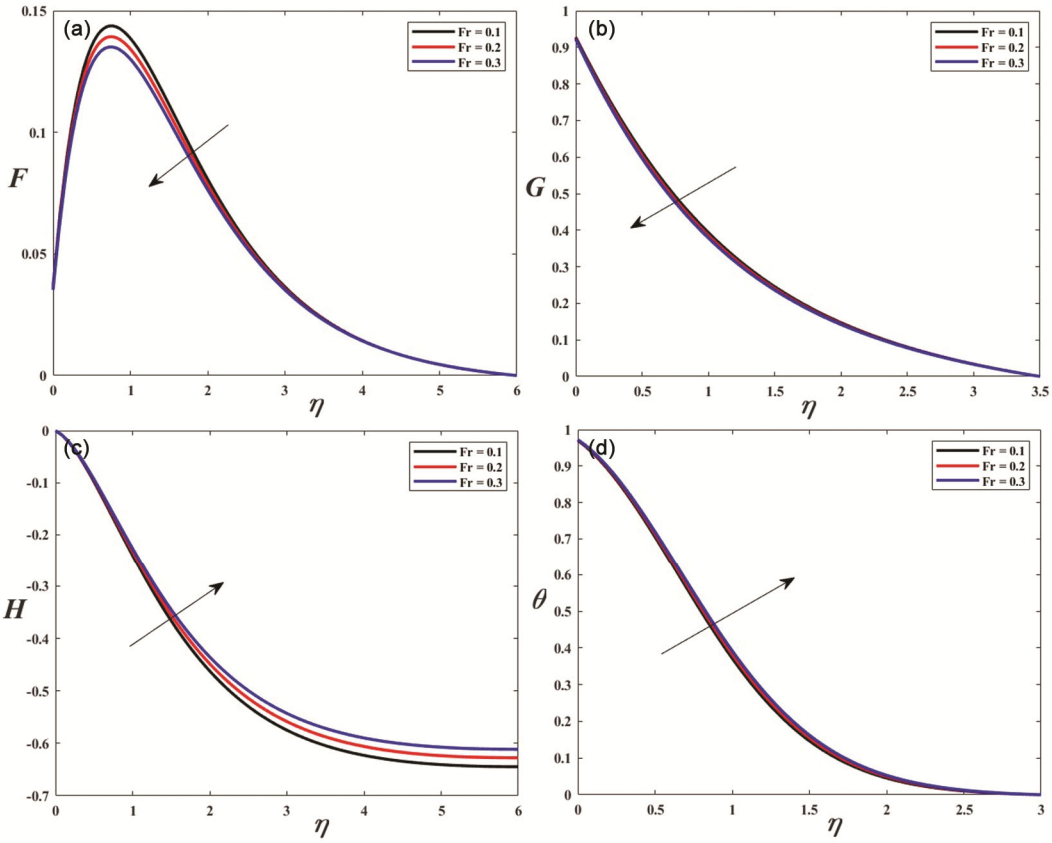

Fig. 8 — (a) Impact of Fr on F (b) Impact of Fr on G (c) Impact of Fr on H; and (d) Impact of Fr on θ

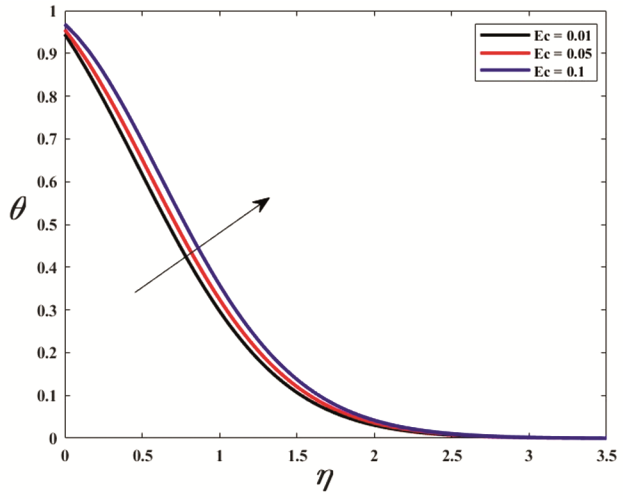

Fig. 9 — Impact of Ec on θ

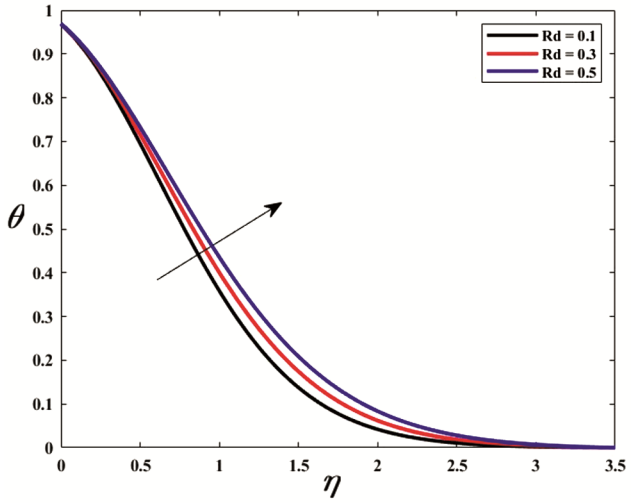

Fig. 10 — Impact of Rd on θ

because thermal radiation adds energy to the system, increasing heat transfer and elevating fluid temperature, thus thickening the thermal boundary layer.

Figure 11 illustrates the effect of the heat source/sink parameter Q on the temperature profile θ. As Q increases, the temperature θ also increases. A positive Q indicates internal heat generation, which boosts the energy within the fluid, resulting in higher temperatures and enhanced thermal thickness near the disk.

Finally, Table 3 presents the influence of various governing parameters on the skin friction coefficient and the Nusselt number for the ternary hybrid

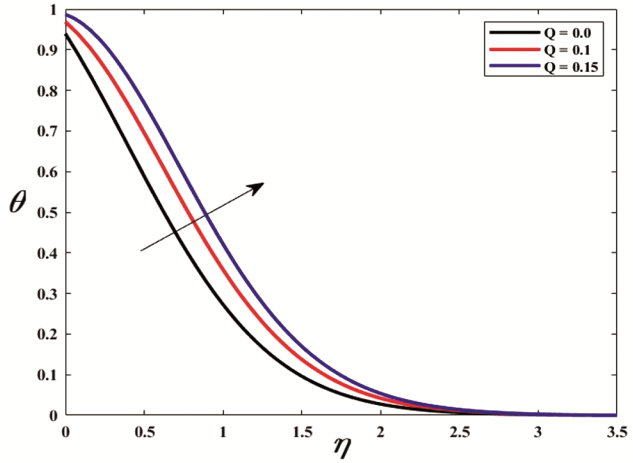

Fig. 11 — Impact of Q on θ

nanofluid. The results indicate that an increase in the nanoparticle volume fractions enhances the heat transfer rate, as evidenced by the rise in the Nusselt number, due to the improved thermal conductivity of the CuO-MoS_2-TiO_2/water mixture. However, this enhancement comes with an increase in viscous drag, reflected by higher values of the skin friction coefficient, attributable to the elevated effective viscosity of the nanofluid. Furthermore, variations in the magnetic field intensity, porosity parameter, and rotational parameter significantly affect both the skin friction and heat transfer rates, underscoring the intricate coupling between magnetic effects, porous medium resistance, and thermal transport mechanisms in the system.

Table 3 — Values of the skin friction coefficient and Nusselt number for different physical parameters in a ternary hybrid nanofluid

M	m	δ	γ	φ	K_1	Rd	Ec	Fr	Q	$(Re)^{\frac{1}{2}}C_f$	$(Re)^{-\frac{1}{2}}Nu$
0.1	0.1	0.1	0.1	0.01	0.1	1.0	0.1	0.1	0.1	0.838358	0.570132
0.5	0.1	0.1	0.1	0.01	0.1	1.0	0.1	0.1	0.1	0.956907	0.319775
1.0	0.1	0.1	0.1	0.01	0.1	1.0	0.1	0.1	0.1	1.106360	0.091455
0.1	0.5	0.1	0.1	0.01	0.1	1.0	0.1	0.1	0.1	0.855243	0.607733
0.1	1.0	0.1	0.1	0.01	0.1	1.0	0.1	0.1	0.1	0.876123	0.651158
0.1	1.5	0.1	0.1	0.01	0.1	1.0	0.1	0.1	0.1	0.896742	0.691047
0.1	0.1	0.0	0.1	0.01	0.1	1.0	0.1	0.1	0.1	0.838358	0.596076
0.1	0.1	0.3	0.1	0.01	0.1	1.0	0.1	0.1	0.1	0.838358	0.524477
0.1	0.1	0.5	0.1	0.01	0.1	1.0	0.1	0.1	0.1	0.838358	0.485592
0.1	0.1	0.1	0.0	0.01	0.1	1.0	0.1	0.1	0.1	0.916460	0.449048
0.1	0.1	0.1	0.3	0.01	0.1	1.0	0.1	0.1	0.1	0.709325	0.678665
0.1	0.1	0.1	0.5	0.01	0.1	1.0	0.1	0.1	0.1	0.612594	0.706139
0.1	0.1	0.1	0.1	0.01	0.1	1.0	0.1	0.1	0.1	0.809508	0.532489
0.1	0.1	0.1	0.1	0.03	0.1	1.0	0.1	0.1	0.1	0.838358	0.570132
0.1	0.1	0.1	0.1	0.05	0.1	1.0	0.1	0.1	0.1	0.866161	0.605809
0.1	0.1	0.1	0.1	0.01	0.1	1.0	0.1	0.1	0.1	0.838358	0.570132
0.1	0.1	0.1	0.1	0.01	0.2	1.0	0.1	0.1	0.1	0.863918	0.514737
0.1	0.1	0.1	0.1	0.01	0.3	1.0	0.1	0.1	0.1	0.891120	0.461623
0.1	0.1	0.1	0.1	0.01	0.1	0.1	0.1	0.1	0.1	0.838358	0.327103
0.1	0.1	0.1	0.1	0.01	0.1	0.3	0.1	0.1	0.1	0.838358	0.382498
0.1	0.1	0.1	0.1	0.01	0.1	0.5	0.1	0.1	0.1	0.838358	0.436250
0.1	0.1	0.1	0.1	0.01	0.1	0.1	0.01	0.1	0.1	0.838358	0.836491
0.1	0.1	0.1	0.1	0.01	0.1	0.1	0.05	0.1	0.1	0.838358	0.718109
0.1	0.1	0.1	0.1	0.01	0.1	0.1	0.1	0.1	0.1	0.838358	0.570132
0.1	0.1	0.1	0.1	0.01	0.1	0.1	0.1	0.1	0.1	0.838358	0.570132
0.1	0.1	0.1	0.1	0.01	0.1	0.1	0.1	0.2	0.1	0.860665	0.553897
0.1	0.1	0.1	0.1	0.01	0.1	0.1	0.1	0.3	0.1	0.882726	0.538312
0.1	0.1	0.1	0.1	0.01	0.1	0.1	0.1	0.1	0.0	0.838358	0.988908
0.1	0.1	0.1	0.1	0.01	0.1	0.1	0.1	0.1	0.1	0.838358	0.570132
0.1	0.1	0.1	0.1	0.01	0.1	0.1	0.1	0.1	0.15	0.838358	0.307403

4 Conclusion

This investigation demonstrated that the combined influence of magnetic fields, porous media resistance, Joule heating, Hall current, and thermal radiation played a pivotal role in shaping the fluid flow and heat transfer characteristics of a CuO-MoS_2-TiO_2/water ternary hybrid nanofluid over a rotating disk. The principal findings are outlined as follows:

i The application of a magnetic field and the presence of porous resistance impeded both radial and tangential velocity components due to enhanced resistive forces, while concurrently elevated the temperature distribution through Joule heating effects.

ii The implementation of velocity slip conditions resulted in diminished radial and tangential momentum transfer, accompanied by a slight enhancement in axial velocity.

iii Thermal slip leads to a reduction in fluid temperature near the surface as it limits conductive heat transfer from the disk.

iv An increase in the Hall current intensified radial velocity but reduced tangential and axial velocities, along with a drop in the fluid temperature.

v The Forchheimer term contributed to elevated axial velocity and temperature by reinforcing inertial drag and promoting energy dissipation within the flow domain.

vi Thermal radiation and internal heat generation significantly enhanced the fluid temperature, contributing to the thickening of the thermal boundary layer.

vii The analysis of skin friction coefficients in both radial and tangential directions revealed substantial sensitivity to slip effects, magnetic field strength, and porous media resistance, which directly impacted wall shear stresses.

viii The Nusselt number, representing the surface heat transfer rate, increased with stronger Joule heating, thermal radiation, and internal heat source, validating the superior thermal efficiency of the ternary hybrid nanofluid.

Overall, the CuO-MoS_2-TiO_2/water ternary hybrid nanofluid demonstrates strong heat transfer performance, confirming its suitability for high-efficiency thermal systems involving rotating and porous components, such as rotating heat exchangers, turbine disk cooling, electromagnetic comparisons show that the ternary hybrid nanofluid enhances the Nusselt number by up to 25 % relative to mono nanofluids and 15 % compared to hybrid nanofluids, while increased nanoparticle loading and thermal radiation further improve heat transfer by 6 to 33 %, highlighting the beneficial synergistic effects of ternary nanoparticles.

Future work may extent the present analysis by incorporating unsteady flow conditions, experimental validation, non-Newtonian base fluids, alternative nanoparticle combinations, and variable thermophysical properties to further evaluate the applicability of ternary hybrid nanofluids in rotating disk systems.

References

1 Mukherjee S, Panda S R, Mishra P C & Chaudhuri P, *Int J Thermophys*, 41 (2020) 1.

2 Preeti, Ojjela O, Kambhatla P K & Mebarek-Oudina F, *Pramana*, 95 (4) (2021) 182.

3 Shanmugam S K, Arivendan A, Govindan Selvamani S, Dheivasigamani T, Sundaresan T K & Ali S, *Ceramics*, 6 (4) (2023) 1926.

4 Rahman K U, Adnan, Mishra N K & Bani-Fwaz M Z, J *Therm Anal Calorim*, 148 (24) (2023) 14385.

5 Riaz M, Khan N, Hashmi M S, Alshomrani A S & Inc, J *Therm Anal Calorim*, 148 (21) (2023) 12285.

6 Gomathy G & Kumar B R, *ZAMM*, 104 (10) (2024) e202300935.

7 Mohana C M & Kumar B R, *ZAMM*, 104 (1) (2024) e202300188.

8 Sarkar A, Mondal H & Nandkeolyar R, *Sci Iran* (2024) 100003.

9 Paul A, Nath J M & Das T K, *ZAMM*, 104 (2) (2024) e202300084.

10 Chakraborty A, Saadeh R, Qazza A, Zomot N, Janapatla P, Khan U, Qraywi M & Muhammad T, *Front Mater*, 11 (2024) 1391377.

11 Jayanthi S & Niranjan H, *Symmetry*, 15 (2) (2023) 314.

12 Hussein U N, Khashi'ie N S, Hamzah K B, Arifin N M & Pop I, *JPHMT*, 37 (6) (2024) 831.

13 Sharma R P, Badak K & Mishra S R, J *Therm Anal Calorim*, 149 (10) (2024) 4913.

14 Aiyashi M A, Abo-Dahab S M & Albalwi M D, *Sci Rep*, 13 (1) (2023) 22529.

15 Mishra S, Swain K & Dalai R, *Iran J Sci Technol Trans Mech Eng*, 48 (2) (2024) 531.

16 Noreen S, Farooq U, Waqas H, Fatima N, Alqurashi MS, Imran M, Akgül A & Bariq A, *Sci Rep*, 13 (1) (2023) 7795.

17 Usman M, Areshi M, Khan N & Eldin MS, *J Therm Anal Calorim*, 148 (17) (2023) 9131.

18 Alqawasmi K, Alharbi K A M, Farooq U, Noreen S, Imran M, Akgül A, Kanan M & Asad J, *Int J Thermofluids*, 18 (2023) 100367.

19 Lone S A, Raizah Z, Alrabaiah H, Shahab S, Saeed A & Khan A, *J Therm Anal Calorim*, 150 (4) (2025) 2651.

20 Mandal G & Pal D, *Int J Numer Methods Heat Fluid Flow*, 35(8) (2025) 2982.

21 Sun T C, DarAssi M H, Bilal M & Khan M A, *Waves Random Complex Media*, 35 (3) (2025) 5802.
22 Sadiya A B & Sucharitha G, *Discover Nano*, 20 (1) (2025) 168.
23 Bartwal R, Rawat S K, Yaseen M & Pant M, *J Braz Soc Mech Sci Eng*, 48 (1) (2026) 4.
24 Sattar A & Ferdows M, *Heat Transfer Phenomena Appli*, *IntechOpen*, (2012) https://doi.org/10.5772/51982.
25 Yin C, Zheng L, Zhang C & Zhang X, *Z Naturforsch, A: Phys Sci*, 70 (5) (2015) 351.
26 Alqahtani A M, Bilal M, Ali A, Alsenani T R & Eldin S M, *Sci Rep*, 13 (1) (2023) 7180.
27 Hussain Z, Aljuaydi F, Ayaz M & Islam S, *Results Eng*, 22 (2024) 102151.
28 Von Kármán T, *Z Angew Math Mech*, 1 (1921) 233.
29 Ramzan M, Kumam P, Lone S A, Seangwattana T, Saeed A & Galal A M, *Heliyon*, 9 (4) (2023) e14875.
30 Faizan M, Ajithkumar M, Reddy M V, Jamal M A, Almutairi B, Shah N A & Chung J D, *Ain Shams Eng J*, 15 (8) (2024) 102839.